EXPERIMENTAL AEROTHERMODYNAMIC RESEARCH

OF HYPERSONIC AIRCRAFT

Technical Progress Report (Substitution)

for the period
October 1, 1988 - March 31, 1989

Submitted to

National Aeronautics and Space Administration
Ames Research Center
Moffett Field, California 94035

Aerothermodynamics Branch
George S. Deiwert, Chief
William K. Lockman, Technical Monitor

NASA-Cooperative Agreement   NCC2-416

Prepared by

ELORET INSTITUTE
1178 Maraschino Drive
Sunnyvale, CA 94087
Phone: (408) 730-8422 and (415) 493-4710
Telefx: 408 730-8422
K. Heinemann, President and Grant Administrator
Joseph W. Cleary, Principal Investigator

7 June, 1989

EXPERIMENTAL AND COMPUTATIONAL FLOW-FIELD RESULTS FOR AN ALL-BODY HYPERSONIC AIRCRAFT (U)

William K. Lockman
NASA Ames Research Center
Moffett Field, California

Joseph W. Cleary
Eloret Institute
Sunnyvale, California

Scott L. Lawrence
NASA Ames Research Center
Moffett Field, California

OUTLINE (U)

(U) The objective, motivation, and approach for this ongoing test program for CFD code validation using the Ames generic all-body hypersonic aircraft model in the Ames 3.5-ft Hypersonic Wind Tunnel (3.5-ft HWT) are stated.

(U) The first section of this paper describes the experimental test program in the 3.5-ft HWT with the all-body model. This includes a description of the model, test conditions, and measurements.

(U) The next section outlines the computational methods currently being applied to the all-body model for this study. These include approximate inviscid methods (tangent-cone, tangent-wedge, swept-cylinder, and an approximation of the hodograph for conical flows) and the UPS code (an upwind parabolized Navier-Stokes solver).

(U) Both experimental and computational results are then given for surface pressure distributions and pitot-pressure surveys with the sharp-nose model at a free-stream Mach number of 7.

(U) Finally, concluding remarks are given concerning the results from the present phase of this test program.

(U) A list of cited references is included.

OUTLINE (U)

(U) OBJECTIVE

(U) EXPERIMENT
- **MODEL**
- **TEST CONDITIONS**
- **MEASUREMENTS**

(U) COMPUTATIONAL METHODS
- **APPROXIMATE INVISCID METHODS**
- **UPS CODE (Upwind PNS Solver)**

(U) RESULTS (Experimental & Computational)
- **SURFACE PRESSURE DISTRIBUTIONS**
- **PITOT-PRESSURE SURVEYS**

(U) CONCLUDING REMARKS

(U) REFERENCES

AMES ALL-BODY HYPERSONIC TEST PROGRAM
FOR CFD CODE VALIDATION (U)

(U) The advanced computer codes being developed for use in the design of such hypersonic aircraft as the National Aero-Space Plane (NASP) require comparisons of the computational results with a broad spectrum of experimental data to fully assess the validity of the codes and to develop confidence in the numerical simulation procedures. This is particularly true for complex flow fields with control surfaces present and for flows with separation, such as leeside flow. Validated codes will be critical to the development of the NASP vehicle.

(U) Therefore, the objective of this ongoing investigation is to establish a benchmark experimental data base for a generic hypersonic vehicle shape for validation and/or calibration of advanced computational fluid dynamics (CFD) computer codes. Hopefully, a more thorough understanding of the flow physics necessary for these codes will also be determined. This is being done by implementing a comprehensive test program for a generic all-body hypersonic aircraft model in the NASA/Ames 3.5-foot Hypersonic Wind Tunnel to obtain pertinent surface and flow-field data over a broad range of test conditions. Flow-visualization results (at free-stream Mach numbers, M_∞, of 5, 7, and 10) and some surface pressure distributions (at M_∞ = 10) were previously presented at NASP Technology Symposia (ref. 1 and 2). Experimental and computational results on surface pressure distributions and pitot-pressure surveys for the sharp-nose model at M_∞ = 7 will be presented in the present paper.

ALL-BODY HYPERSONIC TEST PROGRAM
FOR CFD CODE VALIDATION (U)

(U) OBJECTIVE: Establish benchmark experimental data base for generic hypersonic vehicle shape for validation and/or calibration of advanced CFD computer codes

(U) MOTIVATION: Need for extensive hypersonic data to fully validate CFD codes to be used for NASP & other hypersonic vehicles

(U) APPROACH: Implement comprehensive test program for generic all-body hypersonic aircraft model in Ames 3.5-ft Hypersonic Wind Tunnel to obtain pertinent surface and flow-field data over broad range of test conditions

AMES ALL-BODY HYPERSONIC AIRCRAFT EXPERIMENT (U)
AMES 3.5-FT HWT (U)

(U) The all-body hypersonic aircraft model will be described and shown in the next four figures. The all-body model is representative of a hypersonic cruise vehicle derived from the analytical studies of references 3 to 6. The aerodynamic characteristics of this configuration were previously investigated from subsonic to hypersonic Mach numbers (ref. 7). The present pressure model is larger than the force model of reference 7 (36- versus 19-in. model length) and has 217 surface pressure taps (0.040-in. orifice diameter), of which 192 were connected to electronic pressure scanners installed inside the model for measurements. The all-body model has a delta planform with leading-edge sweepback of 75°. The forebody is an elliptic cone with a major-to-minor axis ratio of 4 and the afterbody has elliptical cross sections with a sharp straight-line trailing edge. This relatively simple model geometry can be easily gridded for CFD codes. The model can be tested with a sharp or blunt nose tip and without or with control surfaces (combination horizontal/vertical tails). The canard will not be used for this hypersonic test program.

ALL-BODY HYPERSONIC AIRCRAFT EXPERIMENT (U)
Ames 3.5-ft HWT (U)

(U) <u>MODEL</u>:

(U) AMES GENERIC ALL-BODY HYPERSONIC MODEL
- **Delta Planform ($\Lambda = 75°$)**
  - **Forebody – Elliptic Cone (a/b = 4)**
  - **Afterbody – Elliptic Cross Sections with Sharp Trailing Edge**
- **Sharp or Blunt Nose Tip**
- **With or Without Control Surfaces**
  - **Canard (Not Used)**
 - **Combination Horizontal/Vertical Tails**

AMES ALL-BODY HYPERSONIC AIRCRAFT MODEL (U)
WITH CONTROL SURFACES (U)

(U) This is a photograph of the complete all-body model with control surfaces (canard and combination horizontal/vertical tails). The support sting for mounting the model in the tunnel is attached to the model along the afterbody centerline.

ALL-BODY HYPERSONIC AIRCRAFT MODEL (U)
WITH CONTROL SURFACES (U)
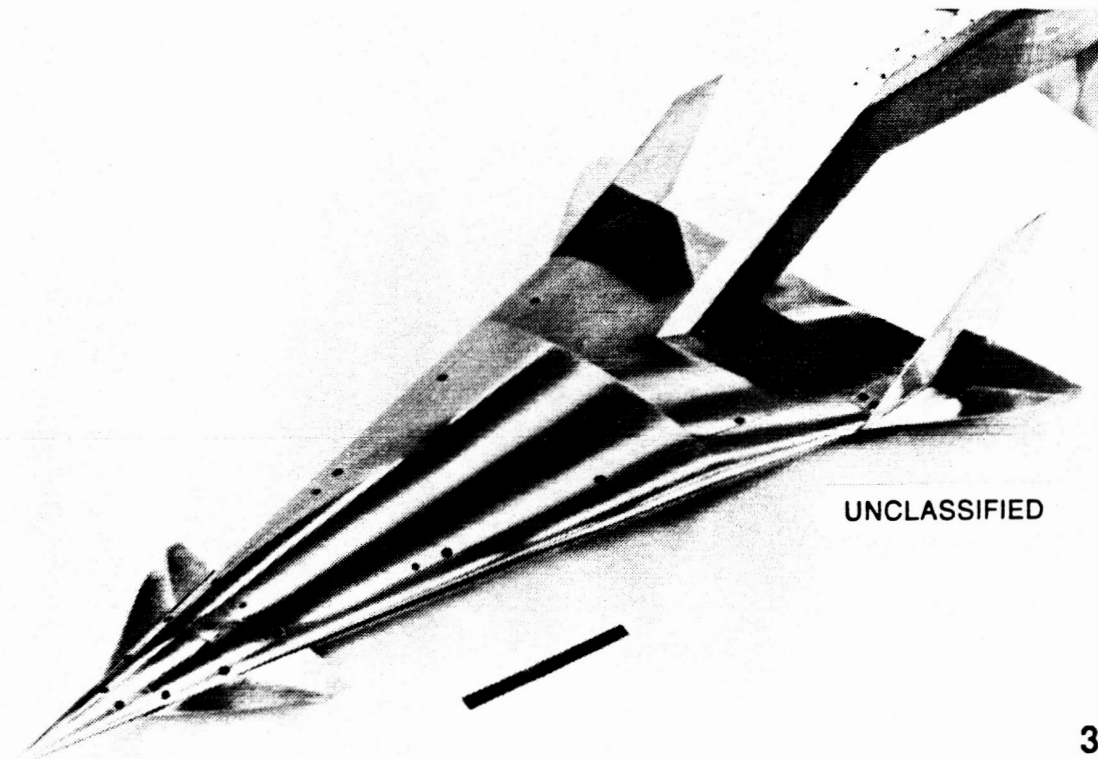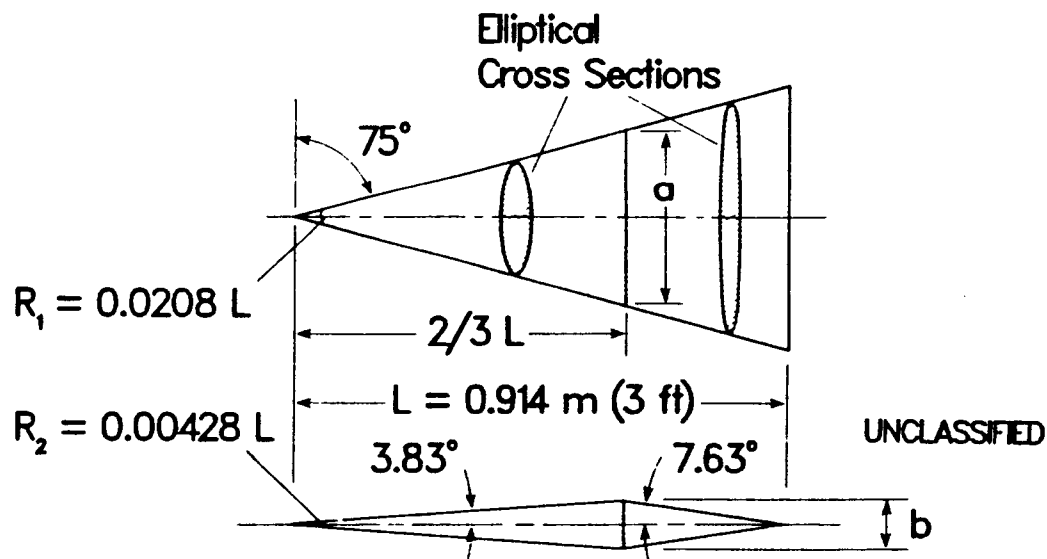
UNCLASSIFIED

37–4

ORIGINAL PAGE
BLACK AND WHITE PHOTOGRAPH

AMES ALL-BODY HYPERSONIC AIRCRAFT MODEL (U)
W/O CONTROL SURFACES (U)

(U)   This is a sketch of the all-body model without control surfaces to show the basic model geometry and dimensions. As previously stated, the model is 3-ft long and has a delta planform with 75° sweepback and elliptical cross sections for both the forebody and afterbody. The juncture between the forebody and afterbody occurs at 2/3 of the body length. The model nose can be either sharp or blunt with the blunt nose blended smoothly into elliptical shape of body. At the vertical symmetry plane, the elliptic-cone forebody has a half angle of only 3.83°, while the elliptic afterbody has a half angle of 7.63°.

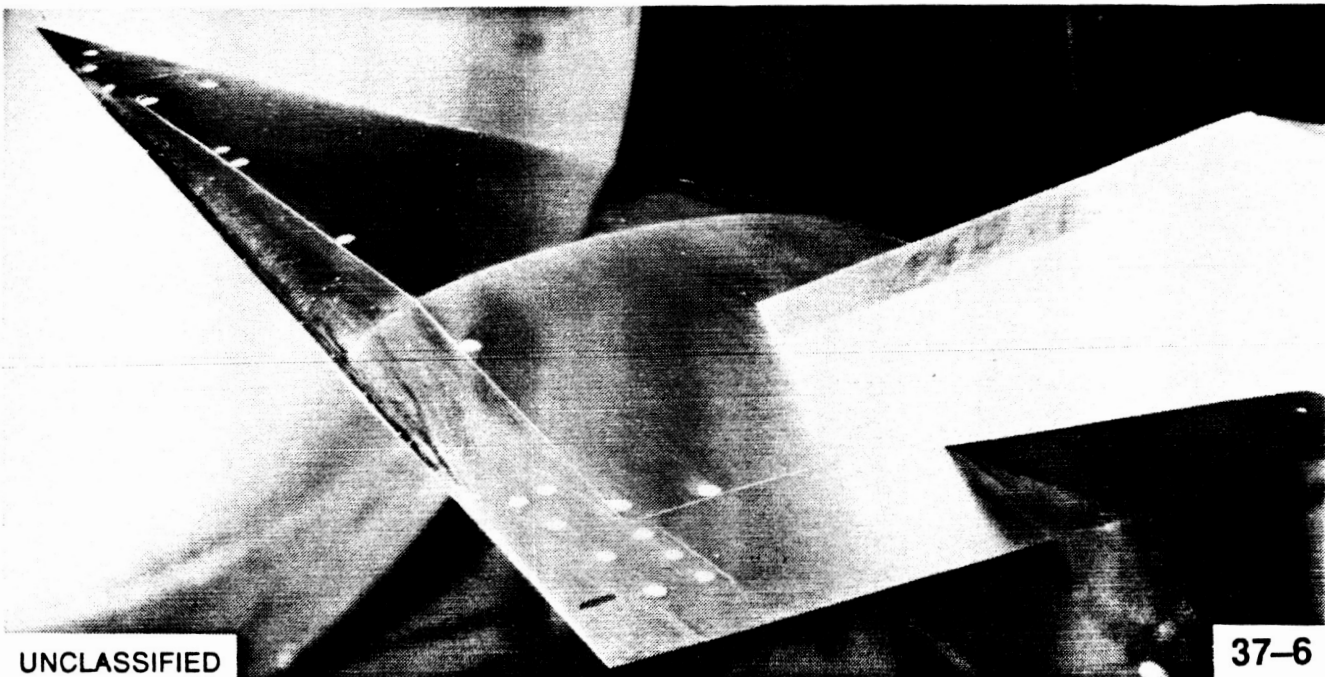# ALL-BODY HYPERSONIC AIRCRAFT MODEL (U)
W/O CONTROL SURFACES (U)

Elliptical
Cross Sections

75°

a

$R_1 = 0.0208\ L$

2/3 L

$R_2 = 0.00428\ L$

L = 0.914 m (3 ft)

3.83°

7.63°

UNCLASSIFIED

b

(U) Forebody — Elliptic Cone (a/b = 4) with Sharp or Blunt Nose Tip
      Afterbody — Elliptical Cross Sections with Sharp Trailing Edge

AMES ALL-BODY HYPERSONIC AIRCRAFT MODEL
IN NASA/AMES 3.5-FT HWT (U)
W/O CONTROL SURFACES; LENGTH = 3 FT (U)

(U) This is a photograph of the all-body model without control surfaces installed in the NASA/Ames 3.5-foot Hypersonic Wind Tunnel. A segment of the circular nozzle exit for the tunnel can be seen ahead of the model. The model support sting exits the top surface of the model afterbody.

(U) The Ames 3.5-foot Hypersonic Wind Tunnel (ref. 8) is a closed-circuit, blowdown-type tunnel with a pebble-bed heater to heat the air to prevent liquefaction and with axisymmetric contoured nozzles to achieve the test Mach numbers. The tunnel is equipped with a model quick-insert mechanism for quickly moving models (transit time as short as 1/2 sec) into and out of the air stream.

ALL-BODY HYPERSONIC AIRCRAFT MODEL
IN NASA/AMES 3.5-FT HWT (U)
W/O CONTROL SURFACES; LENGTH = 3 FT (U)

UNCLASSIFIED

37–6

ORIGINAL PAGE
BLACK AND WHITE PHOTOGRAPH

AMES ALL-BODY HYPERSONIC AIRCRAFT EXPERIMENT (U)
AMES 3.5-FT HWT (U)

(U) The test conditions for this ongoing study will include nominal free-stream Mach numbers, M_∞, of 5, 7, and 10 (Mach 14 nozzle being redesigned.); free-stream Reynolds numbers, $Re_{\infty,L}$, based on model length of 3 ft, from 1.5×10^6 to 25×10^6 (laminar to turbulent flows); and model angles of attack, α, of 0°, 5°, 10°, and 15° (attached and separated flows). For computing the tunnel flow conditions, the air is treated as a thermally perfect, calorically imperfect gas with the relatively small imperfect-gas effects accounted for by the analysis of reference 9. Keyes' equation for viscosity (see ref. 10), rather than Sutherland's equation (ref. 9), is used because of the low free-stream static temperatures (approx 100° R).

(U) For the complete investigation, flow-visualization data (shadowgraphs and surface oil-flow patterns), surface pressures, surface heat transfer, and flow-field surveys (probes and laser velocimetry) will be obtained for the all-body model. The surveys by laser Doppler velocimetry (LDV) are contingent upon a LDV system under development for the 3.5-ft HWT. A study in this facility has demonstrated LDV capability (ref. 11).

(U) Experimental and computational results on surface pressure distributions and pitot-pressure surveys at $M_\infty = 7$ and $Re_{\infty,L} = 15 \times 10^6$ for the basic all-body model (without control surfaces) with a sharp nose tip will be presented in this paper. The windward boundary layer should be turbulent over most of the model length for these conditions. Boundary-layer transition studies using heat-transfer measurements will be conducted to assess this assumption.

ALL-BODY HYPERSONIC AIRCRAFT EXPERIMENT (U)
Ames 3.5-ft HWT (U)

(U) TEST CONDITIONS:
- M_∞ = 5, 7, & 10 (14, when nozzle available)
- $Re_{\infty,L}$ = 1.5×10^6 to 25×10^6 (Laminar to Turbulent Flows)
- α = 0° to 15° (Attached & Separated Flows)

(U) MEASUREMENTS:
- **FLOW VISUALIZATION**
  - Shadowgraphs
  - Surface Oil-Flow Patterns (Skin-Friction Lines)
- **MEAN SURFACE PRESSURES**
- **SURFACE HEAT TRANSFER** (Selected Areas)
- **FLOW-FIELD SURVEYS**
  - Probes (Pitot Pressure)
  - Laser Doppler Velocimetry
    - — Mean Velocities
    - — Turbulence Quantities

COMPUTATIONAL METHODS (U)

(U) Comparisons of the experimental results with computational results from approximate inviscid methods and an upwind parabolized Navier-Stokes code (UPS code) will be shown later. The approximate inviscid methods include simple tangent-cone and tangent-wedge methods (ref. 12) for the windward surfaces, the infinite swept-cylinder method for the leading edge, and an approximation for conical-flow hodographs (ref. 13) for the windward flow field. Although this latter method is semiempirical and the bow shock-wave angle must be known, it yields reasonable estimates of shock-layer properties and wall conditions for inviscid conical flows at hypersonic Mach numbers. These simple inviscid methods are useful tools for providing estimates of the windward pressures. The basic features of the UPS code (ref. 14 and 15) for solving the parabolized Navier-Stokes (PNS) equations will be given in the following figure. Other Navier-Stokes code developers at Ames are also using the all-body configuration for assessment of their codes.

COMPUTATIONAL METHODS (U)

(U) APPROXIMATE INVISCID METHODS:
- **Tangent-Cone**
- **Tangent-Wedge**
- **Swept-Cylinder**
- **Approximation for Conical-Flow Hodograph**

(U) PARABOLIZED NAVIER-STOKES (PNS) CODE:
- **UPS Code (Upwind PNS Solver)**

UPS CODE (U)
(UPWIND PNS SOLVER) (U)

(U) The upwind parabolized Navier-Stokes solver (UPS) code (ref. 14 and 15) employs a numerical algorithm which is second-order accurate and upwind in the crossflow directions. The improved shock-capturing characteristics of the algorithm are due in large part to the upwinding. Presently, the algorithm is first-order accurate in the streamwise direction. The algorithm is implicit both in the interior of the flow field and in the treatment of the boundaries. Finally, the method makes use of the finite-volume approach in order to ensure that fluxes are treated in a conservative manner.

(U) The dissipation of upwind methods allows shock waves to be sharply captured without introducing the oscillations that are typically obtained using conventional central-differencing schemes. Also, because the dissipation is inherent within the algorithm, it is not necessary for the user to specify the values of smoothing parameters.

(U) Presently, there is capability for modeling either laminar or turbulent flow of a perfect gas or equilibrium air. The onset of transition can be specified either as a streamwise station or as a local value of Re_θ/M_e, where Re_θ is the local Reynolds number based on momentum thickness and M_e is the local Mach number at the boundary-layer edge. For all the UPS results presented here, transition was assumed to begin at $x/L = 0.05$ and end at $x/L = 0.1$. The algebraic eddy viscosity turbulence model of Baldwin and Lomax (ref. 14) is presently used. The equilibrium air is modeled using the curve fits of reference 17 for the thermodynamic properties. A version of the code incorporating nonequilibrium air chemistry is being developed at Iowa State University.

UPS CODE (U)
(UPWIND PNS SOLVER) (U)

(U) CHARACTERISTICS OF ALGORITHM:
- **Second-order accurate and upwind in crossflow directions**
- **First-order accurate in streamwise (marching) direction**
- **Implicit**
- **Finite Volume**

(U) ADVANTAGES OF UPWIND SCHEMES:
- **Shock waves are captured sharply and without oscillation**
- **User specification of smoothing parameters is not required**

(U) PRESENT ASSUMPTIONS:
- **Laminar flow**
- **Turbulent flow**
  - **— Boundary-layer transition specified**
  - **— Baldwin-Lomax turbulence model**
- **Perfect gas**
- **Equilibrium air**
- **Version exists for nonequilibrium air**

ALL-BODY CENTERLINE PRESSURES (U)

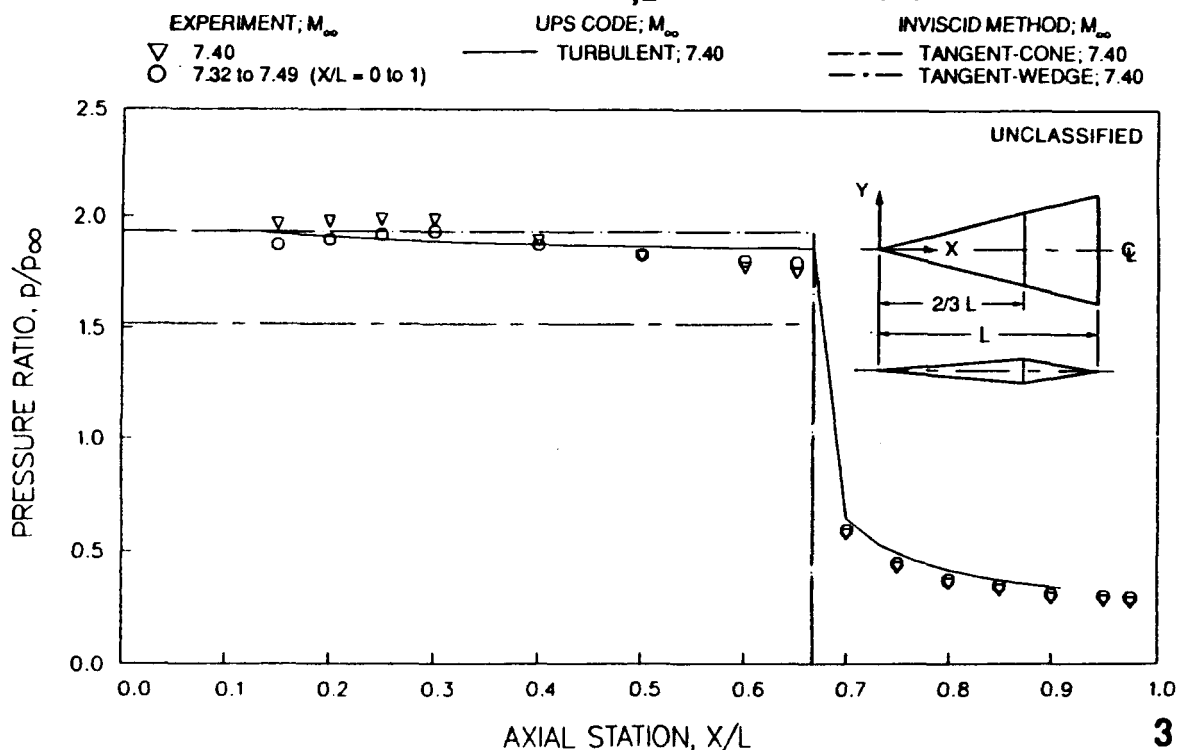$$\alpha = 0°; \; M_\infty = 7.4; \; Re_{\infty,L} = 15 \times 10^6 \quad (U)$$

(U) Both experimental and computational results will now be given in the next several figures for the surface pressure distributions at $\alpha = 0°$ to $15°$ for nominal $M_\infty = 7.4$ and $Re_{\infty,L} = 15 \times 10^6$

(U) In this figure at $\alpha = 0°$, the surface pressure ratio (ratio of surface pressure, p, to free-stream static pressure, p_∞), is plotted versus the axial station, x/L, along the surface centerline for the vertical symmetry plane. To account for an axial Mach-number gradient in the tunnel at $M_\infty = 7$ ($\leq 0.057/ft$) , the experimental surface pressures presented in this and the following figures have all been normalized by p_∞ corresponding to the average M_∞ across the test core at the axial model station for each pressure tap. For example, $M_\infty = 7.32, 7.40$, and 7.49 at x/L = 0.0, 0.5, and 1.0; respectively. The experimental data are also shown in this figure for $M_\infty = 7.40$ to illustrate the improvement to the data with the Mach-number adjustment (pressures are essentially invariant with x/L for conical forebody flow with adjustment). Computations by the inviscid methods and UPS code are given for $M_\infty = 7.40$ (average M_∞ for model at x/L = 0.5).

(U) The large pressure drop at the forebody/afterbody juncture (x/L = 2/3) is quite evident with the pressure further decreasing along the afterbody. The tangent-cone method underestimates the forebody pressure; however, the tangent-wedge estimate is close to these experimental results where surface oil-flow studies indicated wedge-like (strip) surface flow at $\alpha = 0°$ (ref. 1). Of particular significance, the UPS code results for turbulent flow are in good agreement with the experimental data for both the forebody and afterbody.

ALL-BODY CENTERLINE PRESSURES (U)
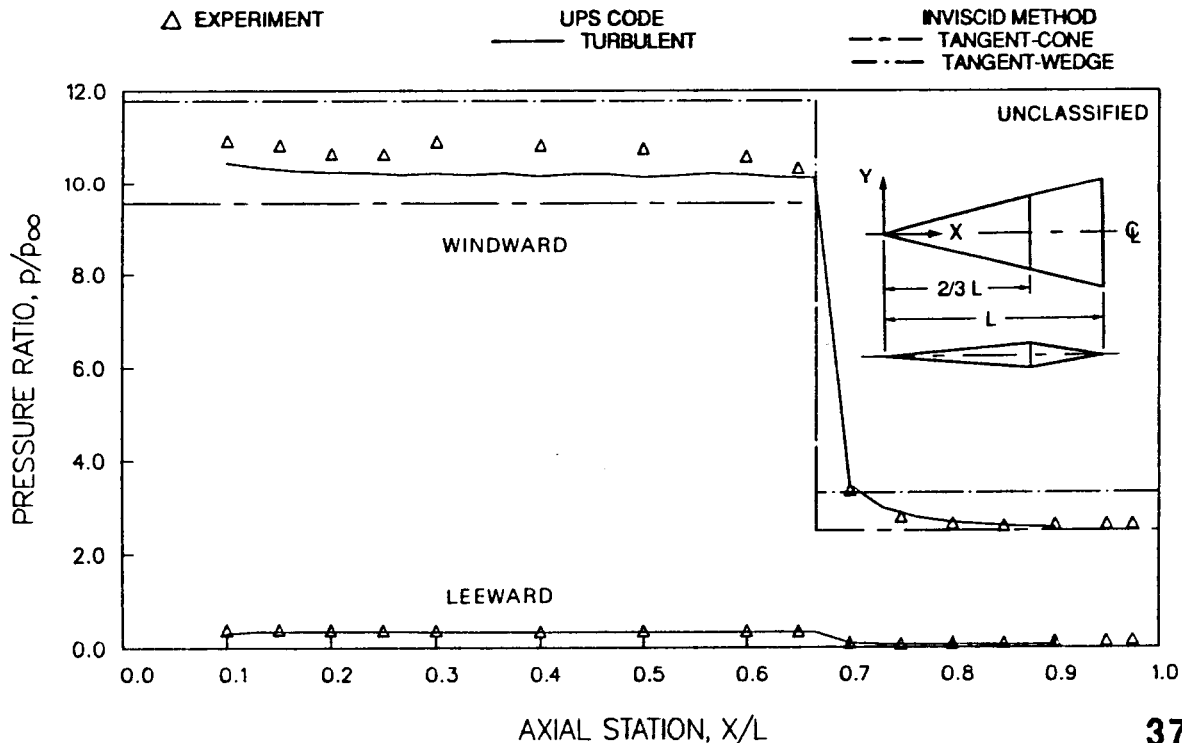### $\alpha = 0°; \; M_\infty = 7.4; \; Re_{\infty,L} = 15 \times 10^6 \quad (U)$

ALL-BODY CENTERLINE PRESSURES (U)
$\alpha = 15°$; $M_\infty = 7.4$; $Re_{\infty,L} = 15 \times 10^6$ (U)

(U) In this figure at $\alpha = 15°$, both the windward and leeward surface pressure ratios, p/p_∞, are plotted versus x/L along the centerline for the vertical symmetry plane. The drop in the windward pressure at the forebody/afterbody juncture (x/L = 2/3) is even more pronounced than at $\alpha = 0°$, and the pressure also decreases along the afterbody. The leeward pressures are significantly lower than the windward pressures and, as for the windward surface, decrease from the forebody to the afterbody. The tangent-cone and tangent-wedge methods yield pressure estimates which bracket the windward data at this angle of attack. The UPS code results for turbulent flow somewhat underpredict the pressures for the windward forebody at this higher angle of attack, but yield good predictions for the windward afterbody and both the leeward forebody and afterbody. The effect of angle of attack on both the windward and leeward centerline pressures will be illustrated in the following two figures, respectively.

ALL-BODY CENTERLINE PRESSURES (U)
$\alpha = 15°$; $M_\infty = 7.4$; $Re_{\infty,L} = 15 \times 10^6$ (U)
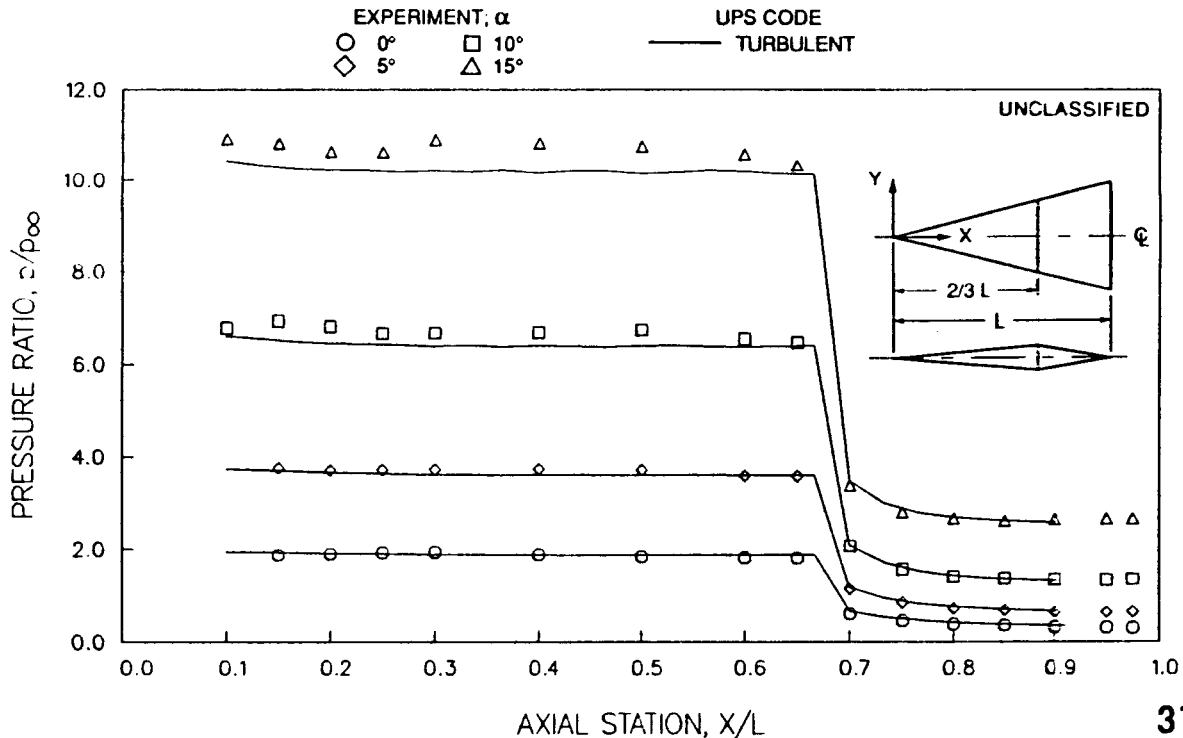
EFFECT OF ANGLE OF ATTACK ON
WINDWARD CENTERLINE PRESSURES (U)

$M_\infty = 7.4$; $Re_{\infty,L} = 15 \times 10^6$ (U)

(U) The effect of angle of attack on the windward centerline pressures is summarized in this figure for $\alpha = 0°, 5°, 10°$, and $15°$. Also shown are predictions of the windward pressures by the UPS code for turbulent flow. The increasing windward pressures with increasing angle of attack and the drop in pressure from the forebody to the afterbody are readily seen. There is generally good agreement between the pressures by the experiment and by the UPS code, with greater differences at the higher angles of attack, as was previously shown for $\alpha = 15°$.

**EFFECT OF ANGLE OF ATTACK ON
WINDWARD CENTERLINE PRESSURES (U)
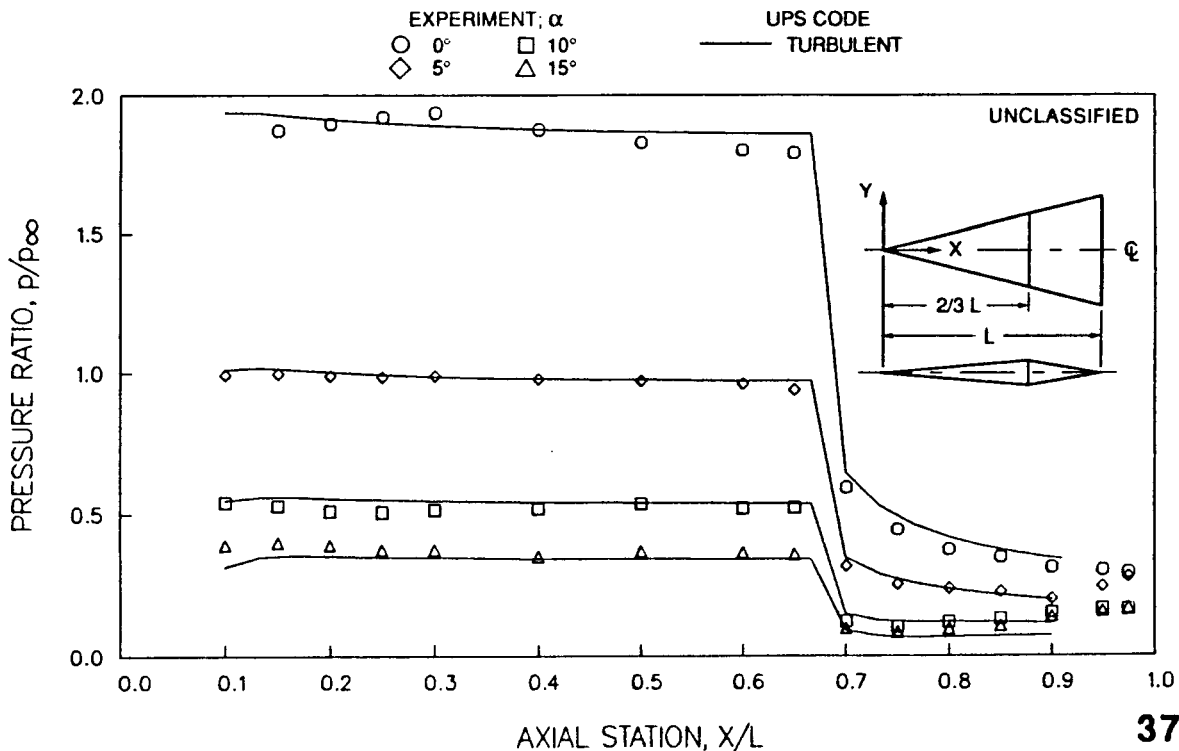$M_\infty = 7.4$; $Re_{\infty,L} = 15 \times 10^6$ (U)**

AXIAL STATION, X/L

37–12

EFFECT OF ANGLE OF ATTACK ON
LEEWARD CENTERLINE PRESSURES (U)

$$M_\infty = 7.4; \; Re_{\infty,L} = 15 \times 10^6 \; \text{(U)}$$

(U) The effect of angle of attack on the leeward centerline pressures is now summarized in this figure for $\alpha = 0°, 5°, 10°$, and $15°$. Also shown are predictions of the leeward pressures by the UPS code for turbulent flow. The decreasing leeward pressures with increasing angle of attack and, as for the windward flow, the drop in pressure from the forebody to the afterbody are readily seen. There is quite good agreement between the pressures by the experiment and by the UPS code, considering the relatively low pressures measured and the complexity of the leeward flow field.

**EFFECT OF ANGLE OF ATTACK ON
LEEWARD CENTERLINE PRESSURES   (U)
$M_\infty = 7.4; \; Re_{\infty,L} = 15 \times 10^6$ (U)**

**37–13**

ALL-BODY LEADING-EDGE PRESSURES (U)
$\alpha = 0°$; $M_\infty = 7.4$; $\mathrm{Re}_{\infty,L} = 15 \times 10^6$ (U)

(U) The pressure ratios along the leading edge at $\alpha = 0°$ are plotted in this figure. Experimental values are shown for both the left and right leading edges which show relatively small differences in the data considering the difficulty of measuring these pressures with the large pressure gradient at the leading edge. Of particular interest are the relatively constant pressures along the conical forebody followed by the decreasing pressures along the nonconical afterbody. The afterbody has some relieving effect on the leading-edge flow because of the decreasing afterbody thickness with increasing x/L. The infinite swept-cylinder method gives a good estimate of the leading-edge pressure for the forebody, while the tangent-cone method overestimates the forebody leading-edge pressures. None of these simple methods correctly estimate the afterbody pressures because they do not account for the changing afterbody geometry. The UPS code results for turbulent flow somewhat overpredict the leading-edge pressure data, but show the correct trend for the afterbody.

ALL-BODY LEADING-EDGE PRESSURES (U)
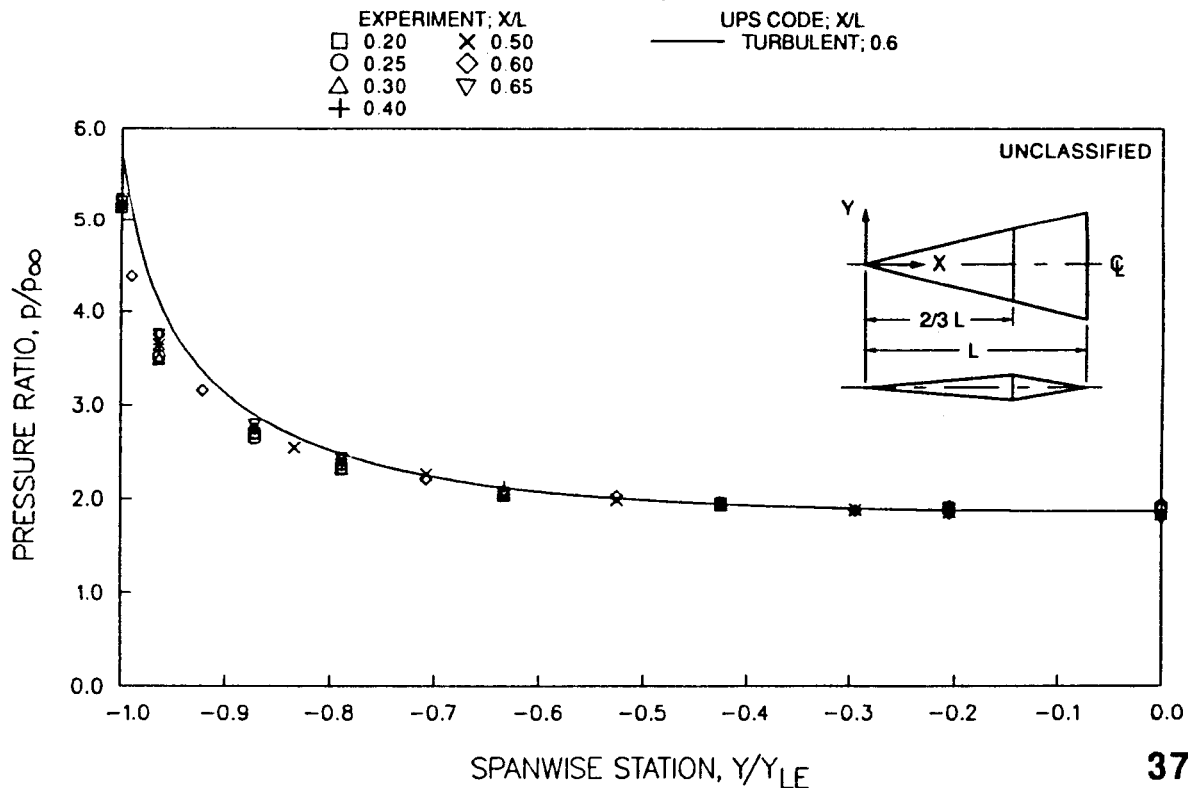$\alpha = 0°$; $M_\infty = 7.4$; $\mathrm{Re}_{\infty,L} = 15 \times 10^6$ (U)
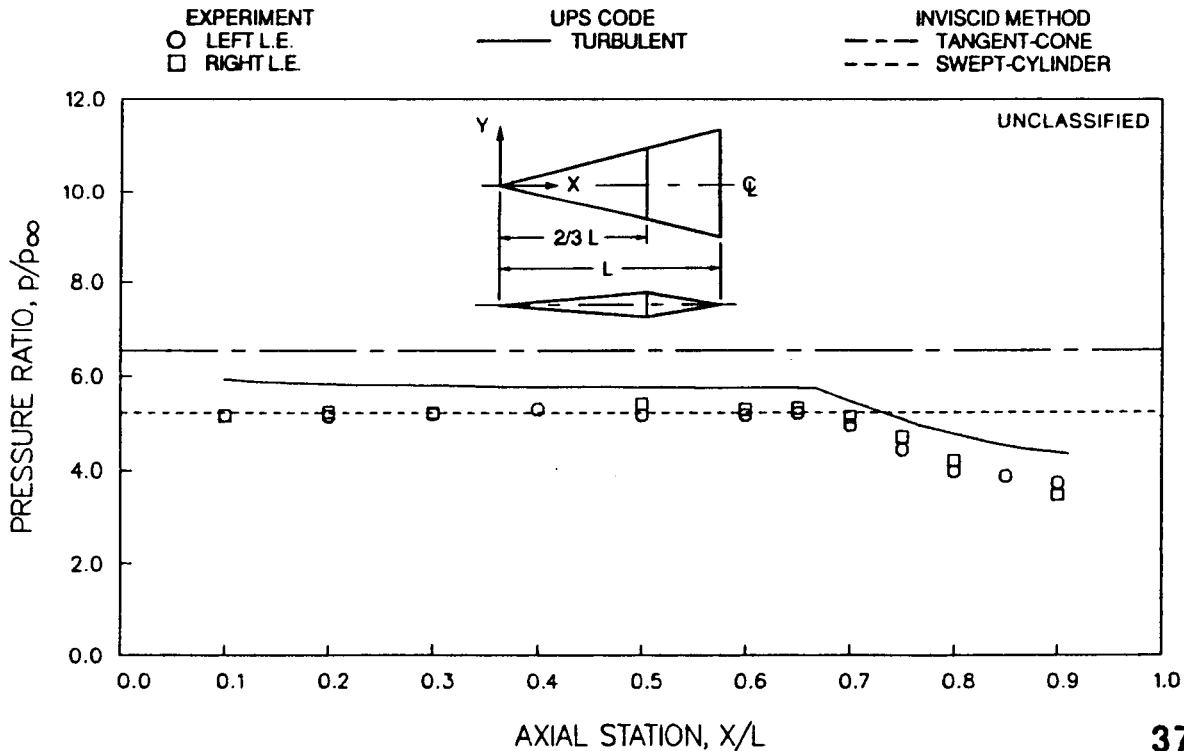
AXIAL STATION, X/L

37–14

SPANWISE PRESSURE DISTRIBUTIONS FOR FOREBODY (U)

$$\alpha = 0°; \quad M_\infty = 7.4; \quad Re_{\infty,L} = 15 \times 10^6 \quad (U)$$

(U) The spanwise pressure distributions for the forebody at $\alpha = 0°$ are plotted in this figure as p/p_∞ versus Y/Y_{LE} for various x/L values, where Y is the spanwise coordinate and Y_{LE} is the value of Y at the leading edge for the given x/L station. Since the pressure taps were primarily on the left (port) side of the model, the results are plotted for negative Y. The data at a given Y/Y_{LE} value for various x/L values are along a conical ray from the nose tip in the planform view of model. The experimental pressures at a given Y/Y_{LE} are essentially invariant with x/L, thus indicating the conical forebody flow. The UPS code results shown at $x/L = 0.6$ for turbulent flow are in good agreement with the corresponding experimental data except for prediction of pressures higher than the experimental values approaching the leading edge.

SPANWISE PRESSURE DISTRIBUTIONS FOR FOREBODY (U)

$$\alpha = 0°; \quad M_\infty = 7.4; \quad Re_{\infty,L} = 15 \times 10^6 \quad (U)$$

EXPERIMENT; X/L		UPS CODE; X/L
□ 0.20	✕ 0.50	——— TURBULENT; 0.6
○ 0.25	◇ 0.60	
△ 0.30	▽ 0.65	
+ 0.40		

SPANWISE STATION, Y/Y_{LE}

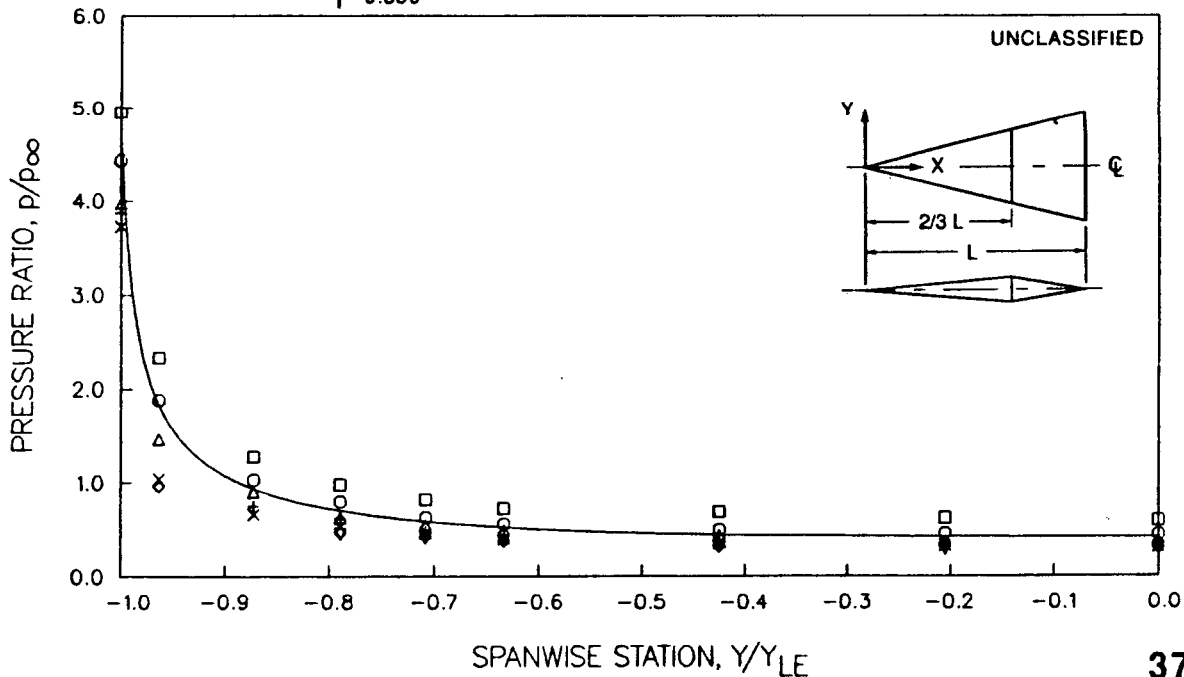## SPANWISE PRESSURE DISTRIBUTIONS FOR AFTERBODY (U)

$$\alpha = 0°; \quad M_\infty = 7.4; \quad Re_{\infty,L} = 15 \times 10^6 \quad (U)$$

(U) The spanwise pressure distributions for the afterbody at $\alpha = 0°$ are now plotted in this figure. As for the forebody, the data at a given Y/Y_{LE} are along a conical ray from the nose tip in the planform view of model. However, unlike for the forebody, the experimental pressures at a given Y/Y_{LE} decrease with increasing x/L, thus indicating the nonconical afterbody flow. By comparing this plot with the forebody plot (Fig. 37-15), the drop in pressure from the forebody to the afterbody is further illustrated. The UPS code results shown at x/L = 0.8 for turbulent flow are in good agreement with the corresponding experimental data at x/L = 0.8, except for differences near the leading edge. Although not shown here, the UPS code turbulent results have the same trend of decreasing pressure with increasing x/L as given by the experimental data.

SPANWISE PRESSURE DISTRIBUTIONS FOR AFTERBODY (U)

$$\alpha = 0°; \quad M_\infty = 7.4; \quad Re_{\infty,L} = 15 \times 10^6 \quad (U)$$

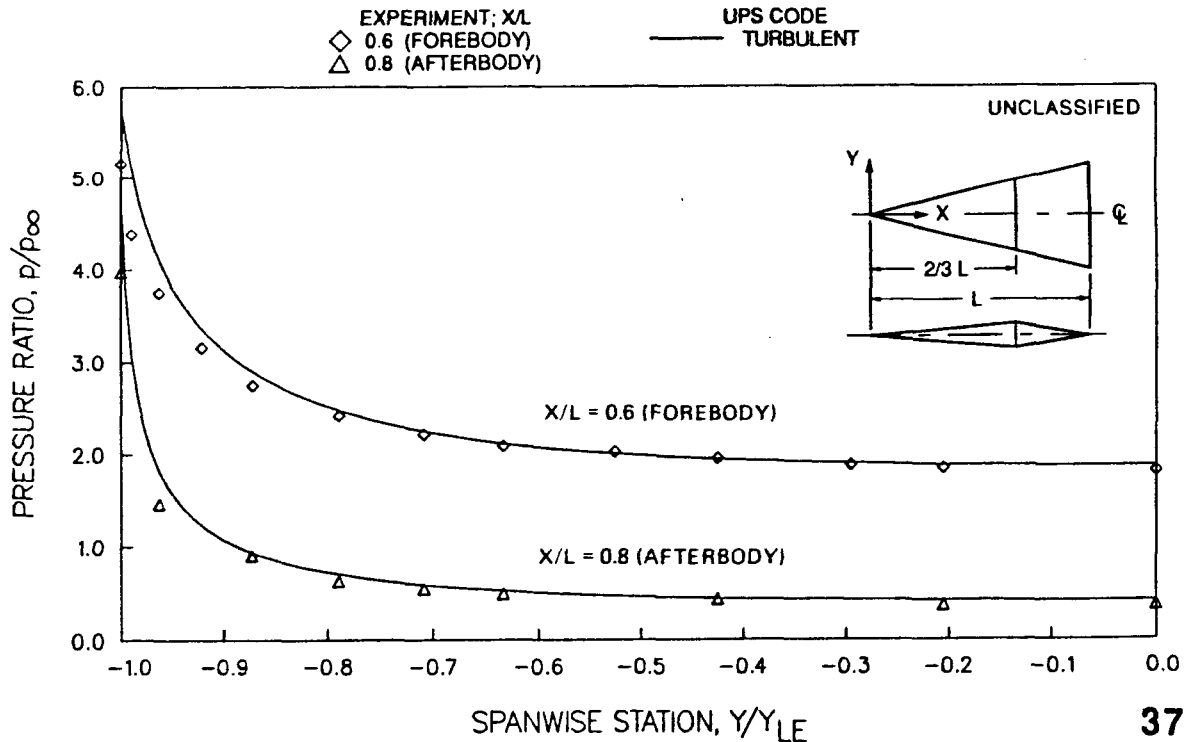| EXPERIMENT; X/L		UPS CODE; X/L
□ 0.700 X 0.900		———— TURBULENT; 0.8
○ 0.750 ◇ 0.950		
△ 0.800 ▽ 0.975		
+ 0.850		

SPANWISE PRESSURE DISTRIBUTIONS FOR
FOREBODY AND AFTERBODY (U)

$\alpha = 0°; \; M_\infty = 7.4; \; Re_{\infty,L} = 15 \times 10^6$ (U)

(U) The spanwise pressure distributions for the forebody and afterbody stations of x/L = 0.6 and 0.8, respectively, at $\alpha = 0°$ are now plotted in this figure to further illustrate the differences between the forebody and afterbody pressures and to show more clearly the comparisons with UPS code computations for these two stations. The forebody/afterbody differences in pressure levels are more readily apparent. The agreement between the experimental and computational results are again seen to be good except approaching the leading edge.

**SPANWISE PRESSURE DISTRIBUTIONS FOR
FOREBODY AND AFTERBODY (U)**

$\alpha = 0°; \; M_\infty = 7.4; \; Re_{\infty,L} = 15 \times 10^6$ (U)

EXPERIMENT; X/L
◇ 0.6 (FOREBODY)
△ 0.8 (AFTERBODY)

UPS CODE
——— TURBULENT

UNCLASSIFIED

X/L = 0.6 (FOREBODY)

X/L = 0.8 (AFTERBODY)

PRESSURE RATIO, p/p_∞

SPANWISE STATION, Y/Y_{LE}

37−17
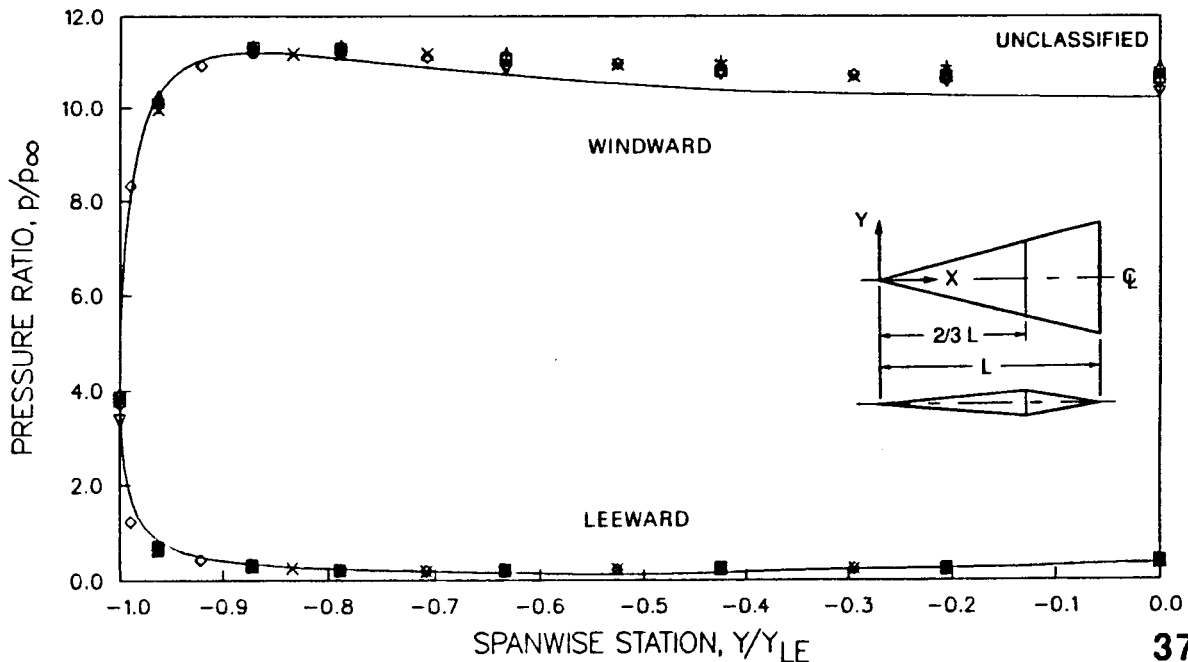
SPANWISE PRESSURE DISTRIBUTIONS FOR FOREBODY (U)

$\alpha = 15°$; $M_\infty = 7.4$; $Re_{\infty,L} = 15 \times 10^6$ (U)

(U) Both the windward and leeward spanwise pressure distributions for the forebody at $\alpha = 15°$ are plotted in this figure. As at $\alpha = 0°$, the forebody pressures are essentially invariant with x/L, thus indicating the conical forebody flow. The UPS code results shown at x/L = 0.6 for turbulent flow are in relatively good agreement with the corresponding experimental data. As was shown for the model centerline at this angle of attack, the UPS code underpredicts the windward pressures toward the centerline.

SPANWISE PRESSURE DISTRIBUTIONS FOR FOREBODY (U)

$\alpha = 15°$; $M_\infty = 7.4$; $Re_{\infty,L} = 15 \times 10^6$ (U)

| EXPERIMENT; X/L		UPS CODE; X/L
□ 0.20	X 0.50	——— TURBULENT; 0.6
O 0.25	◇ 0.60	
△ 0.30	▽ 0.65	
+ 0.40		

SPANWISE PRESSURE DISTRIBUTIONS FOR AFTERBODY (U)
$\alpha = 15°$; $M_\infty = 7.4$; $Re_{\infty,L} = 15 \times 10^6$ (U)

(U) Both the windward and leeward spanwise pressure distributions for the afterbody at $\alpha = 15°$ are plotted in this figure. As was previously shown at $\alpha = 0°$, the afterbody flow is nonconical with the pressures at a given Y/Y_{LE} decreasing with increasing x/L. This is particularly evident by the data for the windward surface. By comparing this plot with the forebody plot at $\alpha = 15°$ (Fig. 37-18) and the plots at $\alpha = 0°$ (Figs. 37-15 and 37-16), the changes in the pressure distributions from the forebody to the afterbody at $\alpha = 15°$ are even more pronounced than at $\alpha = 0°$. The UPS code results shown at x/L = 0.8 for turbulent flow are in good agreement with the corresponding experimental data at x/L = 0.8. Although not shown here, the UPS code turbulent results have the same trend of decreasing pressure with increasing x/L as given by the experimental data.

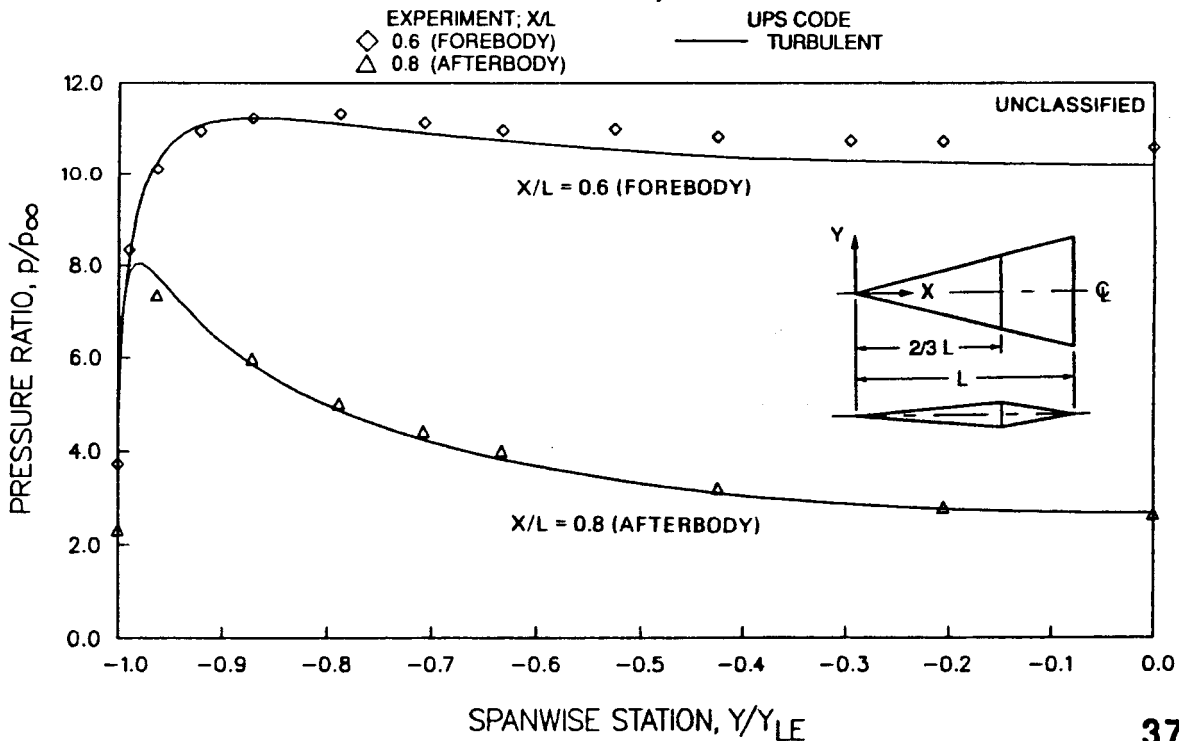## SPANWISE PRESSURE DISTRIBUTIONS FOR AFTERBODY (U)
$\alpha = 15°$; $M_\infty = 7.4$; $Re_{\infty,L} = 15 \times 10^6$ (U)
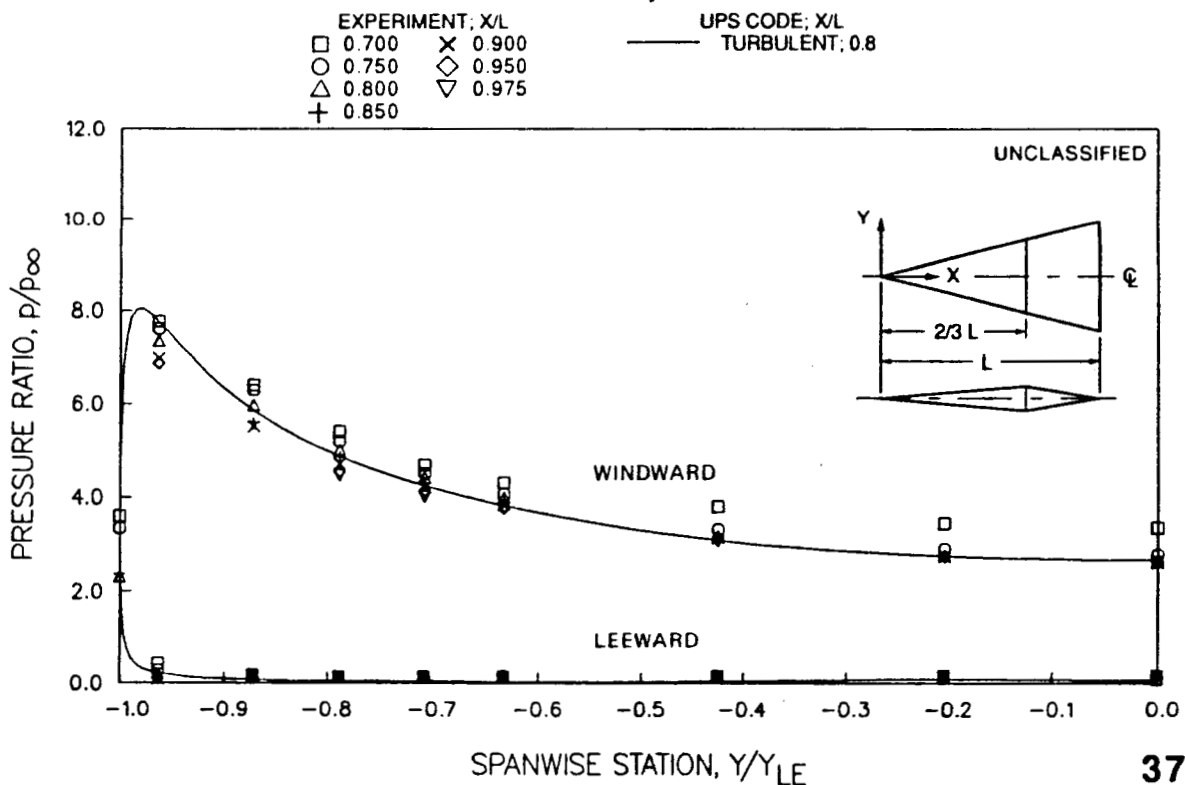
WINDWARD SPANWISE PRESSURE DISTRIBUTIONS FOR FOREBODY AND AFTERBODY (U)

$$\alpha = 15°; \; M_\infty = 7.4; \; Re_{\infty,L} = 15 \times 10^6 \; (U)$$

(U) The windward spanwise pressure distributions for the forebody and afterbody stations of $x/L = 0.6$ and 0.8, respectively, at $\alpha = 15°$ are now plotted in this figure to further illustrate the differences between the forebody and afterbody pressures and to show more clearly the comparisons with UPS code computations for these two stations. The forebody/afterbody differences in pressure levels and distributions are more readily apparent. The agreement between the experimental and computational results are again seen to be good except approaching the forebody centerline.

WINDWARD SPANWISE PRESSURE DISTRIBUTIONS FOR FOREBODY AND AFTERBODY (U)

$$\alpha = 15°; \; M_\infty = 7.4; \; Re_{\infty,L} = 15 \times 10^6 \; (U)$$

SPANWISE STATION, Y/Y_{LE}

37–20

LEEWARD SPANWISE PRESSURE DISTRIBUTIONS FOR FOREBODY AND AFTERBODY (U)

$\alpha = 15°$; $M_\infty = 7.4$; $Re_{\infty,L} = 15 \times 10^6$ (U)

(U) The leeward spanwise pressure distributions for the forebody and afterbody stations of $x/L = 0.6$ and 0.8, respectively, at $\alpha = 15°$ are now plotted in this figure to further illustrate the differences between the forebody and afterbody pressures and to show more clearly the comparisons with UPS code computations for these two stations. The forebody/afterbody differences in these relatively small pressure levels are more readily apparent. The agreement between the experimental and computational results are seen to be good except near midspan for the afterbody and approaching the leading edge.

LEEWARD SPANWISE PRESSURE DISTRIBUTIONS FOR FOREBODY AND AFTERBODY (U)
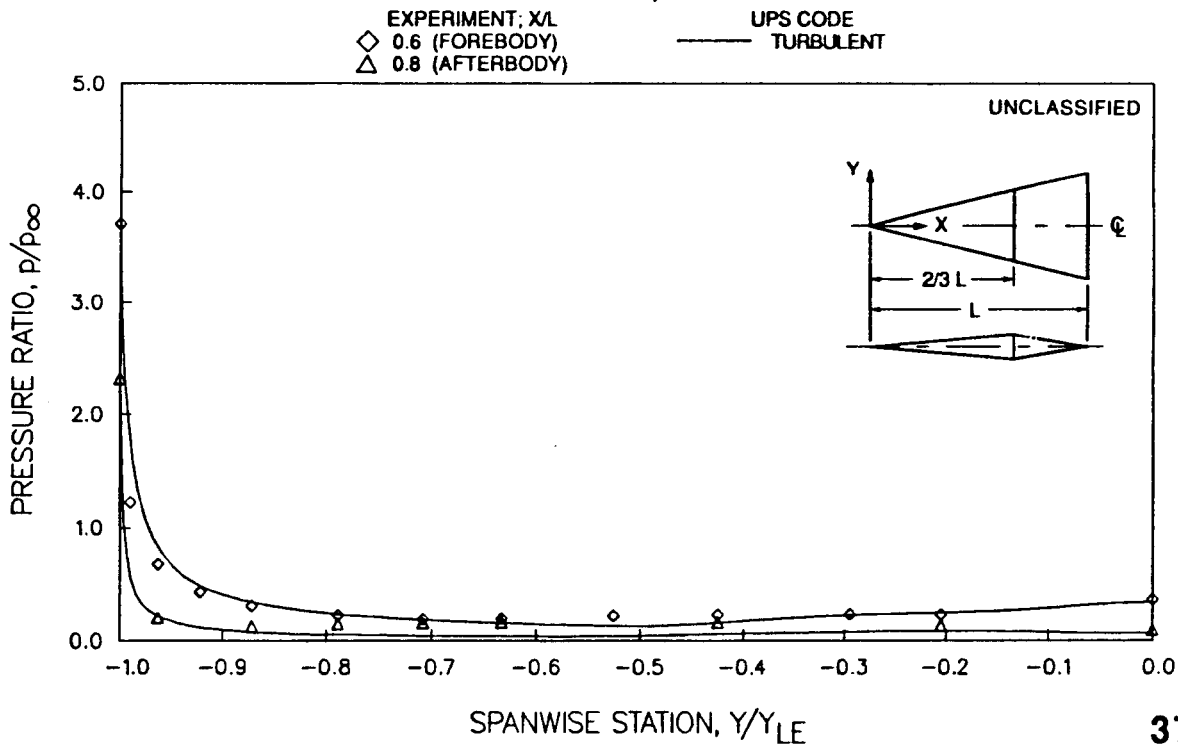
$\alpha = 15°$; $M_\infty = 7.4$; $Re_{\infty,L} = 15 \times 10^6$ (U)

SHADOWGRAPH OF PITOT-PRESSURE SURVEY SETUP (U)
x/L = 0.8; Afterbody Centerline; $\alpha = 15°$; $M_\infty = 7.4$; $Re_{\infty,L} = 15 \times 10^6$ (U)

(U) Pitot-pressure surveys of the flow field were conducted to provide details of the shock layer structure. The remaining figures give experimental and computational results for these surveys. A shadowgraph of the flow over the lower surface of the model and the installation of the pitot-pressure rake at station x/L = 0.8 on model centerline are shown in this figure. The 27 pitot probes of the rake are equally spaced except for the probe adjacent to the model which is bent parallel to the model surface. The probes are stainless steel tubing with an outside diameter of 0.062 in. and an inside diameter of 0.040 in. The bow shock wave is essentially straight as shown by the shadowgraph, and the flow over the forebody can be considered approximately conical. The forebody boundary layer appears to be turbulent under these test conditions.

(U) At the juncture of the forebody and afterbody for the model (x/L = 2/3), an expansion wave is apparent as the flow turns the corner and parallels the afterbody. This expansion wave intersects the bow shock wave downstream in the vicinity of the model trailing edge. Therefore, the bow wave is essentially straight over most of the afterbody. Individual bow waves can be seen on the pitot probes that are outside the boundary layer. Because the flow is turned at the model bow wave, the probes are at only a small angle to the local flow. Thus, the pitot-pressure measurements are not subject to significant errors due to flow angularity.

SHADOWGRAPH OF PITOT-PRESSURE SURVEY SETUP (U)
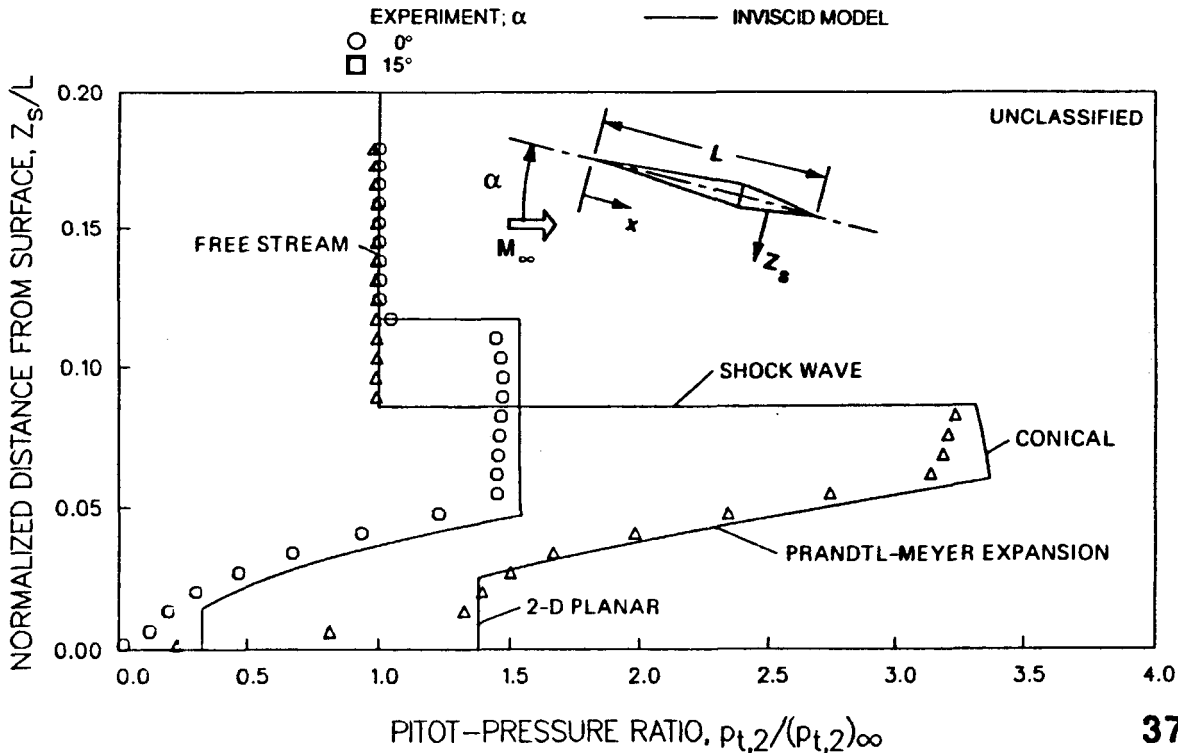x/L = 0.8; Afterbody Centerline; $\alpha = 15°$; $M_\infty = 7.4$; $Re_{\infty,L} = 15 \times 10^6$ (U)
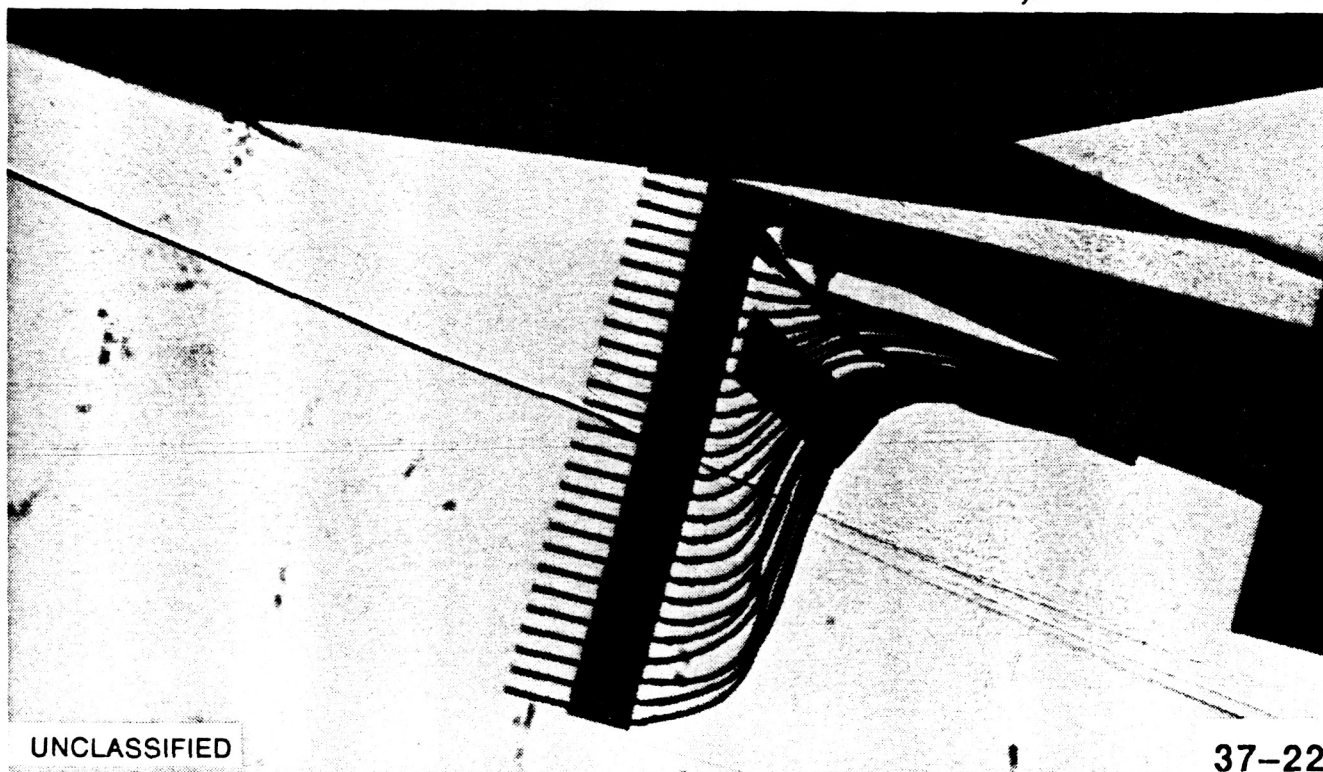
COMPARISON OF EXPERIMENTAL PITOT-PRESSURE DISTRIBUTIONS WITH INVISCID MODEL OF FLOW (U)
x/L = 0.8; Afterbody Centerline; $M_\infty = 7.4$; $Re_{\infty,L} = 15 \times 10^6$ (U)

(U)   The purpose of this figure is to show the basic features of the shock-layer flow on the model lower surface at the rake survey station. Experimental data for $\alpha = 0°$ and $15°$ are compared with a simplified inviscid model of the flow. Pitot pressure (normalized by free-stream pitot pressure) is plotted versus distance from the model surface (normalized by model length). This distance is measured perpendicular to the horizontal symmetry plane of the model (See model sketch on figure.). The inviscid flow model consists of an outer conical-flow region next to the shock wave, a middle region represented by a Prandtl-Meyer expansion, and a 2-D planar region near the surface where the flow turns parallel to the surface.

(U)   To construct the inviscid model, the forebody surface Mach number must be known for calculation of the Prandtl-Meyer expansion. Using the experimental shock-wave angle, the approximate method given in reference 13 was used to calculate the forebody Mach number. The forebody and afterbody local Mach numbers were estimated to be 6.70 and 9.45, respectively, for $\alpha = 0°$, and 4.25 and 5.40, respectively, for $\alpha = 15°$. These values are based on $M_\infty = 7.43$.

(U)   As shown in the figure, the main features of the inviscid model agree well with experiment except near the surface where viscous effects predominate. In the outer region behind the shock wave, the measured pitot pressure agrees well with that by the inviscid model at the wave.

EFFECT OF ANGLE OF ATTACK ON PITOT-PRESSURE DISTRIBUTION AT AFTERBODY STATION (U)

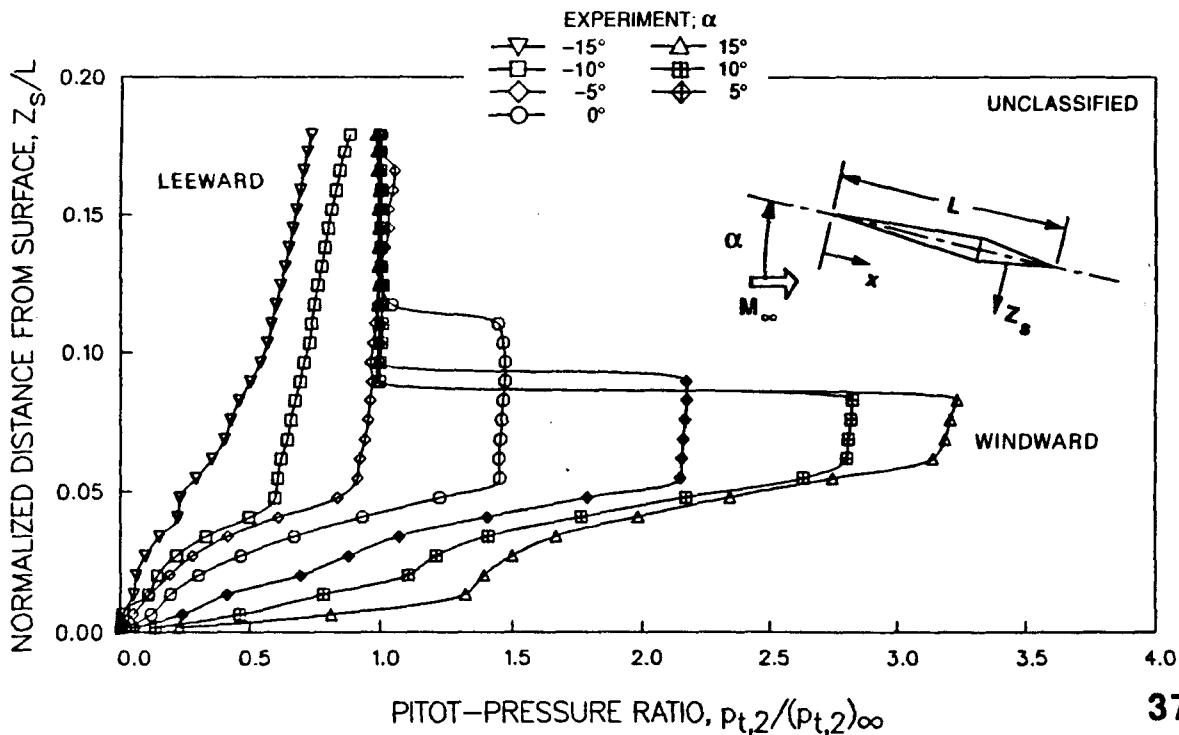$x/L = 0.8$; Centerline; $M_\infty = 7.4$; $Re_{\infty,L} = 15 \times 10^6$ (U)

(U) Experimental measurements of pitot pressure that show the effects of varying angle of attack are given in this figure for an angle-of-attack range of $-15°$ to $15°$ at $x/L = 0.8$. As in the preceding analysis for Fig. 37-23, it is helpful to divide the shock layer into three basic regions. From the figure, it is evident that in the outer region next to the shock wave, the pitot-pressure distribution differs from that characterized by inviscid conical flow since the pitot pressure decreases with decreasing Z_s/L. The phenomenon is more evident with increasing α. This needs clarification and will be investigated with the planned LDV flow-field surveys. The central expansion and inner viscous regions are evident for the entire angle-of-attack range.

(U) The shock-layer thickness decreases with increasing angle of attack except for $\alpha = 10°$ and $15°$ where the thickness is about the same. For $\alpha = -5°$, the shock wave crosses the rake near the end with only a slight increase in pitot pressure from that in the free stream, thus indicating that the leeward wave angle approaches that of a Mach wave. For $\alpha = -10°$ and $-15°$, the wave is beyond the rake.

(U) On the windward side ($\alpha \geq 0°$), the incremental increase in pitot pressure, for a constant incremental increase in α, decreases with increasing α in the outer flow region. This agrees with oblique-shock theory for a two-shock system (bow shock and pitot-probe shock) as the bow-shock wave angle increases with increasing α.

EFFECT OF ANGLE OF ATTACK ON PITOT-PRESSURE DISTRIBUTION AT AFTERBODY STATION (U)
$x/L = 0.8$; Centerline; $M_\infty = 7.4$; $Re_{\infty,L} = 15 \times 10^6$ (U)

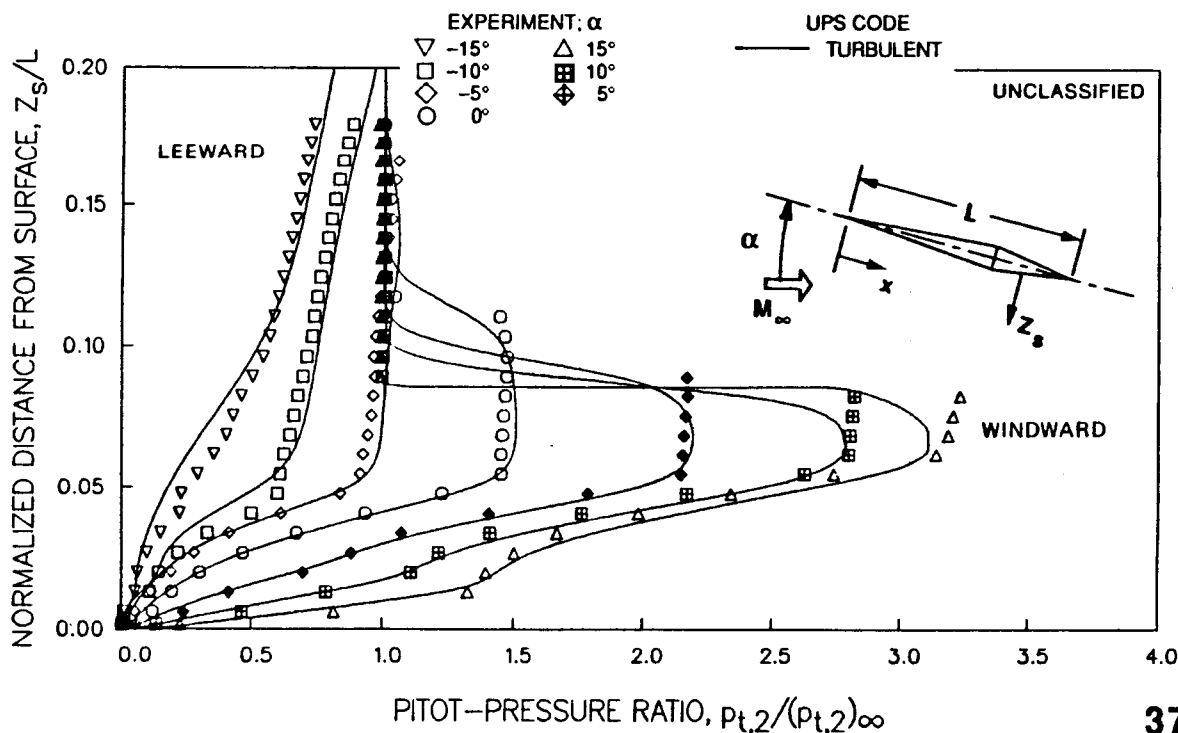## EXPERIMENTAL AND COMPUTATIONAL PITOT-PRESSURE DISTRIBUTIONS AT AFTERBODY STATION (U)

x/L = 0.8; Centerline; $M_\infty = 7.4$; $Re_{\infty,L} = 15 \times 10^6$ (U)

(U) The experimental pitot-pressure measurements are now compared in this figure with computations by the UPS code for turbulent flow. Comparisons are made for both the windward and leeward flows. For windward flow ($\alpha \geq 0°$), the computations agree well with the experimental measurements except near the bow wave, which is not accurately defined by these computations due to the coarseness of the grid used in the outer flow. Planned use of adaptive grids with the UPS code should help resolve the flow near the bow wave. The pitot-pressure level in the outer flow region is predicted well by the code. It is also significant that the UPS code predicts the inner viscous and expansion regions of the flow accurately. For $\alpha > 0°$, the "S-shaped" variation of pitot pressure for the region where the viscous layer merges with the expansion is reproduced by the code.

(U) On the leeside ($\alpha < 0°$), the computations predict the main trends of the experimental data for all three angles of attack, with some differences in the details for the higher negative angles of attack ($\alpha = -10°$ and $-15°$). For $\alpha = -5°$, there is good agreement between the experiment and the UPS code computations for the inner region. It is clear that the leeward viscous flow over the all-body model is highly complex and additional computations and experiments are needed. Flow-field tests are now being initiated for other axial and spanwise locations, including the forebody.

EXPERIMENTAL AND COMPUTATIONAL PITOT-PRESSURE DISTRIBUTIONS AT AFTERBODY STATION (U)
x/L = 0.8; Centerline; $M_\infty = 7.4$; $Re_{\infty,L} = 15 \times 10^6$ (U)

COMPUTATIONAL PITOT-PRESSURE DISTRIBUTIONS
## AT FOREBODY AND AFTERBODY STATIONS (U)
Centerline; $M_\infty = 7.4$; $Re_{\infty,L} = 15 \times 10^6$ (U)

(U) In anticipation of experimental pitot-pressure measurements on the forebody from this ongoing study, pitot-pressure distributions were computed by the UPS code to show the shock-layer and boundary-layer characteristics for the forebody. Computations of pitot-pressure distributions at x/L = 0.6 are compared in this figure with results given previously for the afterbody at x/L = 0.8 ($\alpha = -15°, 0°$, and 15°). On the forebody windward surfaces ($\alpha = 0°$ and 15°), the distributions are basically conical except for the viscous region near the surface where the boundary-layer thickness is about 15 percent of the shock-layer thickness. As might be expected, the expansion from the forebody/afterbody juncture creates major changes in the conical-type forebody distributions and in the boundary-layer characteristics.

(U) Leeward ($\alpha = -15°$) for both the forebody and afterbody , the pitot-pressure distributions appear to be nonconical. This is due to the thickened viscous layer with embedded vortices that is characteristic of sharp conical bodies at higher angles of attack, and evident from the previous flow-visualization results for the all-body model (ref. 1 and 2) . As shown in reference 18 for delta wings, this viscous layer is mainly below a line projected from the nose tip in the free-stream direction, which for the present case is at $Z_s/L = 0.12$.

COMPUTATIONAL PITOT-PRESSURE DISTRIBUTIONS
AT FOREBODY AND AFTERBODY STATIONS (U)
Centerline; $M_\infty = 7.4$; $Re_{\infty,L} = 15 \times 10^6$ (U)

UPS CODE, TURBULENT; X/L
- - - - 0.6 (FOREBODY)
——— 0.8 (AFTERBODY)
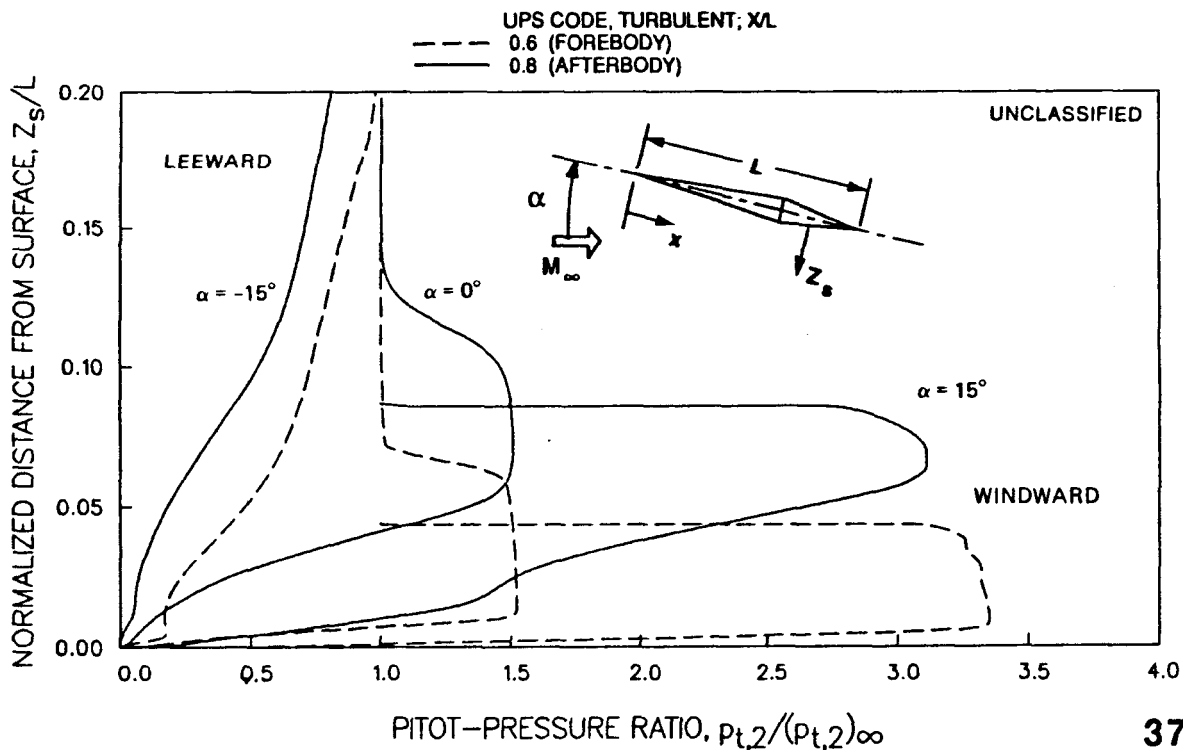
CONCLUDING REMARKS (U)

(U) This paper defined a comprehensive test program being implemented in the NASA/Ames 3.5-foot Hypersonic Wind Tunnel for obtaining data on a generic all-body hypersonic vehicle for CFD code validation; outlined computational methods (approximate inviscid methods and an upwind parabolized Navier-Stokes code) currently being applied to the all-body model; and presented experimental and computational results on surface pressure distributions and pitot-pressure surveys for the basic sharp-nose model (without control surfaces) at a free-stream Mach number of 7.

CONCLUDING REMARKS (U)

(U) DEFINED ONGOING EXPERIMENT IN AMES 3.5-FT HWT WITH ALL-BODY MODEL

(U) OUTLINED COMPUTATIONAL METHODS USED TO DATE

(U) PRESENTED EXPERIMENTAL & COMPUTATIONAL RESULTS:
- **SURFACE PRESSURE DISTRIBUTIONS**
  - Significant changes from forebody (conical) to afterbody (nonconical) flows.
  - Generally good agreement observed between pressures by experiment and by UPS code. (Some differences at higher angles of attack and near leading edge.)
- **PITOT-PRESSURE SURVEYS**
  - Significant changes in profiles at given model station with changes in angle of attack.
  - Significant changes in profiles from forebody to afterbody.
  - Good agreement observed between experiment & UPS code computations for viscous and expansion portions of shock layer. (Some differences for leeward flow at higher angles of attack)

REFERENCES (U)

(U) 1. Lockman, William K.; Lawrence, Scott L.; and Cleary, Joseph W.: Flow Visualization Results for an All-Body Hypersonic Aircraft. Third National Aero-Space Plane Technology Symposium, Paper No. 6, June 1987.

(U) 2. Lockman, William K.; Cleary, Joseph W.; and Lawrence, Scott L.: Flow Visualization and Pressure Distributions for an All-Body Hypersonic Aircraft. Fourth National Aero-Space Plane Technology Symposium, Paper No. 53, Feb. 1988.

(U) 3. Gregory, Thomas J.; Wilcox, Darrell E.; and Williams, Louis J.: The Effects of Propulsion System – Airframe Interactions on the Performance of Hypersonic Aircraft. AIAA Paper 67-493, July 1967.

(U) 4. Gregory, Thomas J.; Williams, Louis J.; and Wilcox, Darrell E.: The Airbreathing Launch Vehicle for Earth Orbit Shuttle – Performance and Operation. AIAA Paper 70-270, Feb. 1970.

(U) 5. Gregory, Thomas J.; Ardema, Mark D.; and Waters, Mark H.: Hypersonic Transport Preliminary Performance Estimates for an All-Body Configuration. AIAA Paper 70-1224, Oct. 1970.

(U) 6. Williams, Louis J.: Estimated Aerodynamics of All-Body Hypersonic Aircraft Configurations. NASA TM X-2091, 1971.

(U) 7. Nelms, Walter P., Jr.; and Thomas, Charles L.: Aerodynamic Characteristics of an All-Body Hypersonic Aircraft Configuration at Mach Numbers from 0.65 to 10.6. NASA TN D-6577, 1971.

(U) 8. Penaranda, Frank E.; and Freda, M. Shannon; eds.: Aeronautical Facilities Catalogue, Volume I, Wind Tunnels. NASA RP-1132, 1985.

(U) 9. Ames Research Staff: Equations, Tables, and Charts for Compressible Flow. NACA Report 1135, 1953.

(U) 10. Bertram, Mitchel H.: Comment on "Viscosity of Air." J. Spacecraft & Rockets, vol. 4, no. 2, Feb. 1967. pp. 287–288.

(U) 11. Owen, F. K. and Horstman, C. C.: An Assessment of Laser Velocimeter Potential in Hypersonic Flow. Fourth National Aero-Space Plane Technology Symposium, Paper No. 13, Feb. 1988.

(U) 12. Hayes, Wallace D. and Probstein, Ronald F.: Hypersonic Flow Theory. Academic Press, Inc., 1959.

(U) 13. Cleary, Joseph W.: Approximation for Distribution of Flow Properties in the Angle-of-Attack Plane of Conical Flows. NASA TN D-5951, 1970.

(U) 14. Lawrence, S. L.; Chaussee, D. S.; and Tannehill, J. C.: Application of an Upwind Algorithm to the Three-Dimensional Parabolized Navier-Stokes Equations. AIAA Paper 87-1112, June 1987.

(U) 15. Lawrence, Scott L. and Balakrishnan, A.: UPS Code Development. Fifth National Aero-Space Plane Technology Symposium, Paper No. 13, Oct. 1988.

(U) 16. Baldwin, B. S. and Lomax, H.: Thin-Layer Approximation and Algebraic Model for Separated Turbulent Flows. AIAA Paper 78-257, Jan.1978.

(U) 17. Srinivasan, S.; Tannehill, J. C.; and Weilmuenster, K. J.: Simplified Curve Fits for the Thermodynamic Properties of Equilibrium Air. NASA RP 1181, Aug. 1987.

(U) 18. Cross, E. J. and Hankey, W. L.: Investigation of the Leeward Side of a Delta Wing at Hypersonic Speeds. AIAA Paper 68-675, June 1968.

37-28